

Diego Vera Sepúlveda¹, Rodrigo Cassineli Palharini¹, Emanuela Gaglio² & Raffaele Savino³

¹Departamento de Ingeniería Mecánica, Universidad Técnica Federico Santa María, Santiago, Chile

²Scuola Superiore Meridionale, Largo S. Marcellino 10, I-80138 Napoli, Italy

³University of Naples "Federico II", Department of Industrial Engineering-Aerospace Section, 80 P. le V. Tecchio, Naples 80125, Italy

Abstract

In the present work, an aerodynamic analysis of an umbrella-like deployable heat shield is investigated for satellite reentry and recovery applications. The influence of altitude in the flowfield structure over the satellite coupled with the deployable heat shield is discussed in detail. Due to the gas rarefaction found at 200, 150, and 100 km altitudes, the Direct Simulation Monte Carlo (DSMC) method is employed in all computations. The study covers macroscopic properties such as flow velocity, temperature, mass density, and pressure, with a detailed analysis of the shock wave structure and thermal gradients around the capsule. Results indicate significant differences in flow behavior and thermal effects, comparing the results obtained at different altitudes. A high diffuse shock is formed upstream of the heat shield at high altitudes with significant thermal gradients due to increased rarefaction. These findings provide insights into the design and analysis of reentry vehicles under rarefied conditions.

Keywords: Deployable heat Shield, CubeSats, Reentry, Direct simulation Monte Carlo

1. Introduction

In recent years, the surge in space missions has been propelled by significant technological advancements and cost reductions [1]. Among the various innovations, CubeSats, which are small modular satellites, have emerged as a cost-effective and efficient solution for many scientific, commercial, and educational applications [2]. However, a primary challenge associated with these devices is their atmospheric reentry and the subsequent safe recovery on Earth. [3]

Deployable Heat Shields (DHSs) have been introduced to tackle this challenge. These devices, which inflate to increase the satellite's surface area and aerodynamic drag, are ingeniously designed to slow down satellites during reentry, shielding them from the intense heat and forces generated by atmospheric friction [4]. Equipped with aerodynamic control systems, such as flaps, DHSs enable precise control over the CubeSat's trajectory and deceleration, thus facilitating a safer and more controlled recovery [5].

The behavior of rarefied flows at high altitudes during atmospheric reentry presents a formidable challenge for traditional computational fluid dynamics (CFD) methods. Rarefied flows, characterized by low particle density, result in less frequent and more random molecular interactions, leading to behavior that eludes the continuous description provided by the Navier-Stokes equations. The Direct Simulation Monte Carlo (DSMC) method, which employs a molecular physics-based approach, simulates these interactions stochastically, thereby capturing the dispersed nature of rarefied flows. [6]

In this research, the DSMC method was employed using the dsmcFoam+ [7] code to investigate the impact of altitude on the flow structure around a DHS equipped with a fin-based control system, specifically tailored for the reentry of a 16U CubeSat [8]. Simulations were performed at altitudes of

100, 150, and 200 km to discern how rarefied flow characteristics, such as shock wave formation and temperature, pressure, and density distributions, are affected.

The study also included a rigorous validation process for the dsmcFoam+ code by benchmarking the results obtained for the flow around the Apollo capsule against the experimental data of Moss [9]. This validation confirmed the code's capability to accurately resolve hypersonic rarefied flows, thereby supporting our simulations' reliability for CubeSat atmospheric reentry.

The document is structured as follows: initially, the theoretical framework and methodology are presented, including an in-depth description of the DSMC method and the dsmcFoam+ code. This is followed by a detailed account of the code's validation process and a presentation of the comparative results. Subsequently, the findings from the simulations at various altitudes are discussed, and the alterations in flow structure and its properties are analyzed. The document concludes with a discussion of the implications of these findings for the design and development of thermal protection and deceleration systems for CubeSats, as well as directions for future research.

2. Computational method

In general, there are two ways to model a flow: assuming it is a continuum that is infinitely divisible and modeling only its macroscopic properties (Continuous Models), or considering its molecular behavior and interactions at that scale, thus obtaining microscopic properties (Molecular Models). Depending on the complexity of the flow to be analyzed and its properties, there are a series of methods in each of these two categories. For molecular models, we encounter deterministic or probabilistic methods, while for continuous models, we encounter methods that solve the Navier-Stokes, Burnett, or Euler equations [10]. This classification is shown in Figure 1.

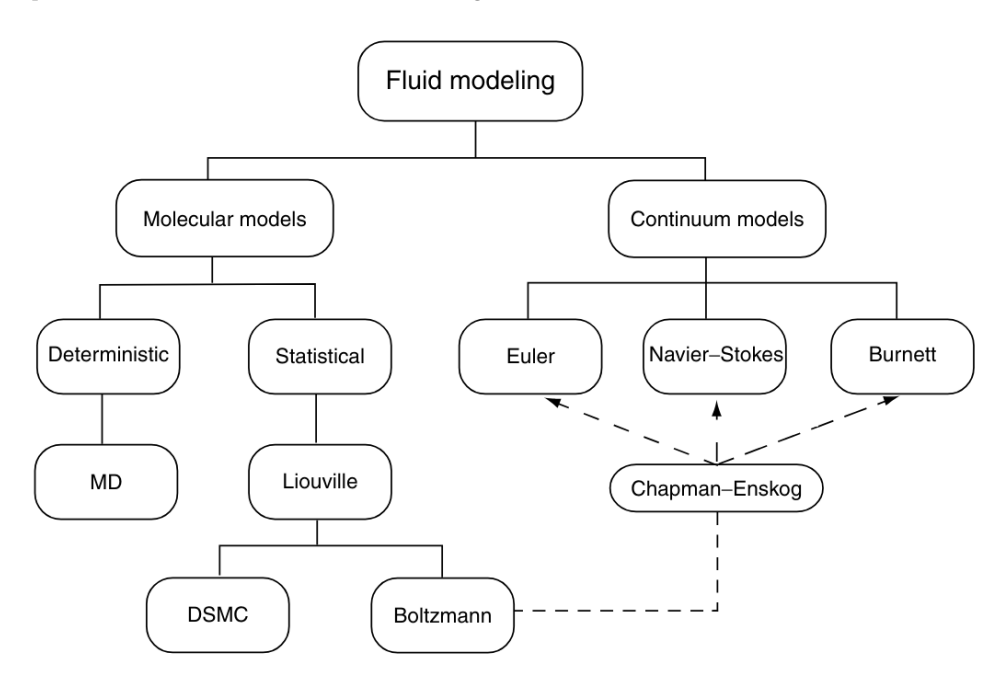


Figure 1 – Flow simulation models. [10]

The most commonly used methods nowadays are continuous models, which rely on the Navier-Stokes equations. After certain approximations and considerations in preprocessing, these models provide sufficiently accurate results for most cases at a considerably lower computational cost than molecular models. However, these methods do not apply to all flows because they operate on the assumption of continuity, not considering interactions at small scales. Therefore, in certain cases, it is imperative to resort to molecular models considering phenomena at microscopic scales [10].

A series of physical values, such as the mean free path and the Knudsen number, must be defined to define each method's validity range.

The mean free path is the average distance molecules travel before colliding with another. This is usually experimentally obtained data but, for an ideal gas modeled with rigid spheres, λ is related to the temperature T and the pressure p as:

$$\lambda = \frac{1}{\sqrt{2}\pi nd^2} = \frac{k_b T}{\sqrt{2}\pi pd^2} \tag{1}$$

where n is the molecular density, d is the molecular diameter, and k_B is the Boltzmann constant. On the other hand, the Knudsen number is defined as the ratio between the mean free path and the characteristic length.

$$Kn = \frac{\lambda}{L} \tag{2}$$

This dimensionless number is an indicative parameter of the rarefaction of a flow and allows an understanding of the number of collisions that occur in a certain volume. This is the determining factor in selecting the simulation model, as shown in Figure 2.

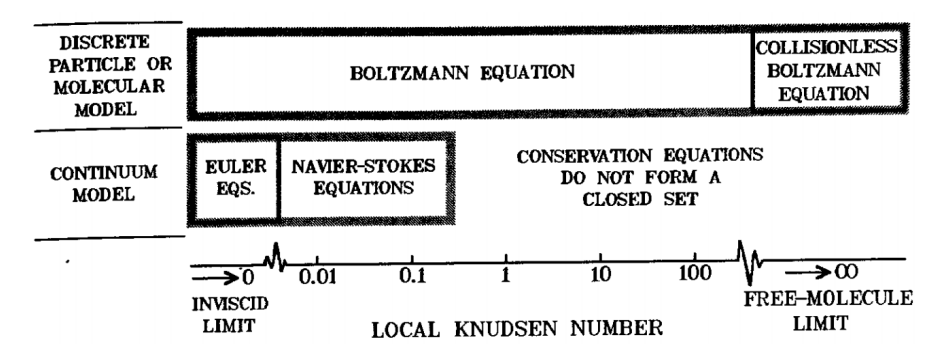


Figure 2 – Knudsen number and fluid simulation models. ([6]

It can be noted that for Knudsen numbers greater than 0.1, continuous models cannot be resolved and thus are not applicable in rarefied flows. On the other hand, molecular models are applicable for any Knudsen number value (computational cost has to be considered), making them the method to use when working with rarefied flows.

Within this framework, it is also important to note that there are different levels of rarefaction represented in different regimes. These depend on the system's Knudsen number, as seen in Figure 3.

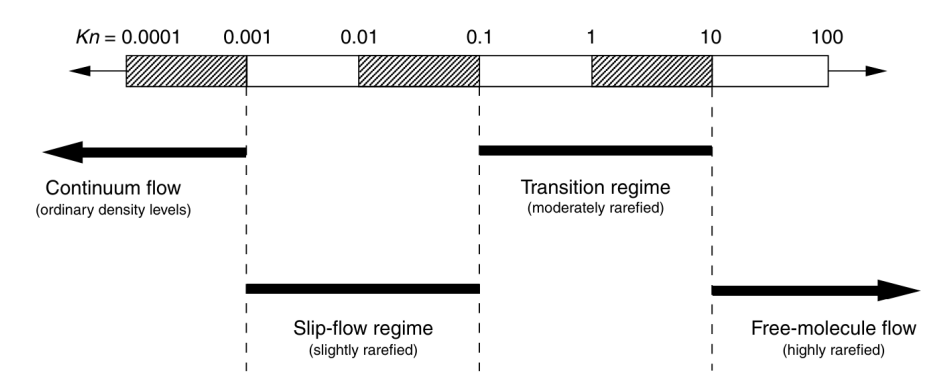


Figure 3 – Simulation scales. [10]

This study presents hypersonic flow at high altitudes, resulting in rarefied flow under different regimes. Finding a computational method capable of simulating this flow type poses a challenge.

Molecular models are used to study fluids by considering them as systems composed of individual particles. These models are divided into two main categories: deterministic and probabilistic.

Deterministic models follow the precise trajectories of each molecule based on their interactions with other molecules and boundary conditions. However, these models are inefficient when applied to rarefied flows, where molecular interactions are relatively infrequent. Therefore, they are mainly used in applications with dense liquids and gases at very small scales.

Statistical models determine the collision probability between simulated particles, while the position and velocity are deterministically obtained. These models are based on the fraction of molecules

in a specific position and state, and their independent variables are time, spatial coordinates, and molecular velocities. To simplify, we consider monoatomic gases without internal degrees of freedom and constraints related to intermolecular distance and thermodynamic equilibrium.

Binary elastic collisions between molecules in a gas are essential in studying gas behaviors. In these collisions, particles have no internal energy exchange, meaning that the total kinetic energy before the collision equals the total kinetic energy after the collision [6].

If two molecules are considered in a plane, each with its velocity and moving along trajectories defined by their velocities. After a collision, the final velocities can be calculated based on the initial velocities and other parameters. To understand the collision, concepts such as the center of mass of the system are used, a kind of "midpoint" that considers the masses and positions of the molecules. Momentum and energy are conserved before and after the collision. Therefore, the final velocities of the molecules depend on the velocity of the center of mass and the relative velocity between the molecules before the collision.

In a reference frame centered in the center of mass, the initial and final velocities are antiparallel to each other. Additionally, the magnitude of the relative velocity remains unchanged due to the collision. Then, the process of determining the final velocities is divided into five steps:

- 1. The velocity of the center of mass of the system is calculated.
- 2. The relative velocity before the collision is calculated.
- 3. The deflection angle, which describes how velocities change after the collision, is calculated.
- 4. The relative velocities after the collision are calculated.
- 5. Finally, the individual velocities of the molecules after the collision are obtained.

In summary, binary elastic collisions are fundamental to understanding how molecules interact in a gas and how these interactions affect their velocities and trajectories. This process is based on principles of conservation of momentum and energy [6].

It is a simplified representation of molecular collisions in a gas. In this model, molecules are considered as solid spheres with a fixed size, and collisions between them occur only when the spheres physically overlap, i.e., when the distance between the centers of the spheres is equal to the sum of their radius. There is no interaction between molecules outside of this physical contact, and collisions are instantaneous and elastic, without exchange of translational or internal energy [6].

The distance between centers and the collision distance for the HS model are defined as:

$$d_{12} = \frac{1}{2}(d_1 + d_2) \tag{3}$$

where d_1 and d_2 are the diameters of the spheres.

2.0.1 Variable Hard Sphere (VHS) Model

It is an extension of the HS model designed to address conditions in which the assumptions of the HS model may not adequately represent the real behavior of gas molecules. Instead of considering all molecules with the same fixed size, the VHS model allows the size of rigid spheres to vary based on c_r through a power law:

$$d = d_{ref} \left(\frac{c_{r,ref}}{c_r}\right)^{\nu} \tag{4}$$

where d is the diameter of the sphere, d_{ref} and $c_{r,ref}$ are reference values, and v is the coefficient of the power law.

Collision sampling techniques in DSMC, such as the Time Counting (TC) method and the No-Time Counting (NTC) method, are based on acceptance-rejection statistics described by Bird [6]. The collision probability P is determined by the relationship between the relative velocity c_r and the total collision cross-section σ_T :

$$P = \frac{\sigma_T c_r}{(\sigma_T c_r)_{max}} \tag{5}$$

In the TC method, a time increment (δt) is assigned to each collision, defined as:

$$\delta t = \frac{2}{N_m \sigma_T c_r} \tag{6}$$

where N_m is the number of simulated molecules per cell.

For the NTC method, a permitted number of collisions (N_{cp}) is performed, determined by:

$$N_{cp} = \frac{N_m \bar{N}_m S_m (\sigma_T c_r)_{max} \Delta t_d}{2Vc}$$
 (7)

Here, Sm is the number of real molecules that a simulated molecule represents, and Vc is the cell volume. Both methods are efficient, chosen according to the specific conditions of the problem. Finally, the solver used for the calculations in this study is dsmcFoam+ [7], an open-source code written in C++ and implemented in OpenFOAM. This tool allows for the resolution of complex geometries in both 2D and 3D, enabling parallelization with as many cores as desired. The code supports the simulation of reactive and non-reactive flows with multiple chemical species, various configurations for collision models and sampling, among other capabilities that make it ideal for this type of study.

2.1 Direct Simulation Monte Carlo (DSMC) Method

For the case addressed in this study, it is necessary to use a statistical molecular model, the chosen one being the Direct Simulation Monte Carlo (DSMC) method. This is a particle simulation technique based on kinetic gas theory. It was developed by Bird in 1976 [6] and has found applications in low-pressure flows and microfluidics.

Since a standard gas volume of $10~[\mu m^3]$ contains a large number of molecules (around 2.69×10^{10} under standard conditions), simulating all molecular interactions is computationally expensive. Therefore, in DSMC, a relatively small number of simulated particles are used, each representing a number of real gas molecules. These particles follow the movement of real particles and experience intermolecular collisions probabilistically to modify their positions and states over time.

The DSMC method is based on the separation of molecular movement and intermolecular collisions, using time intervals shorter than the average time between collisions. The space is divided into cells, similar to finite volume methods, with cell sizes proportional to the mean free path. Then, molecular properties are temporally and spatially averaged at the center of the cells to obtain macroscopic values.

The algorithm used by the method can be seen in Figure 4. Here can be seen that for each time iteration in the DSMC simulation, five fundamental processes are carried out [11], These are described below:

- 1. Initialization: The DSMC simulation begins with predefined initial conditions. In this phase, particles are distributed in the computational domain with initial velocities assigned based on the equilibrium distribution. Although, in the context of a steady-state problem, initial conditions do not affect the final solution, they do influence the computation time. Initial parameters such as position, velocity, collision cross-section, and molecular temperature are crucial for the subsequent evolution of the system.
- 2. **Movement:** During a time interval Δt_d , simulated particles undergo displacement. This displacement is modeled deterministically, with the application of boundary conditions on solid surfaces. The interaction of particles with surfaces is governed by conservation laws and specific boundary conditions. New particles may enter or exit the domain, and their properties are randomly determined based on Δt_d and the macroscopic properties of the boundaries.
- 3. **Indexing:** Since the new positions of particles may be located in different computational cells after their movement, reindexing is necessary to track their trajectory. An efficient indexing and tracking process is essential, especially in large-scale applications.

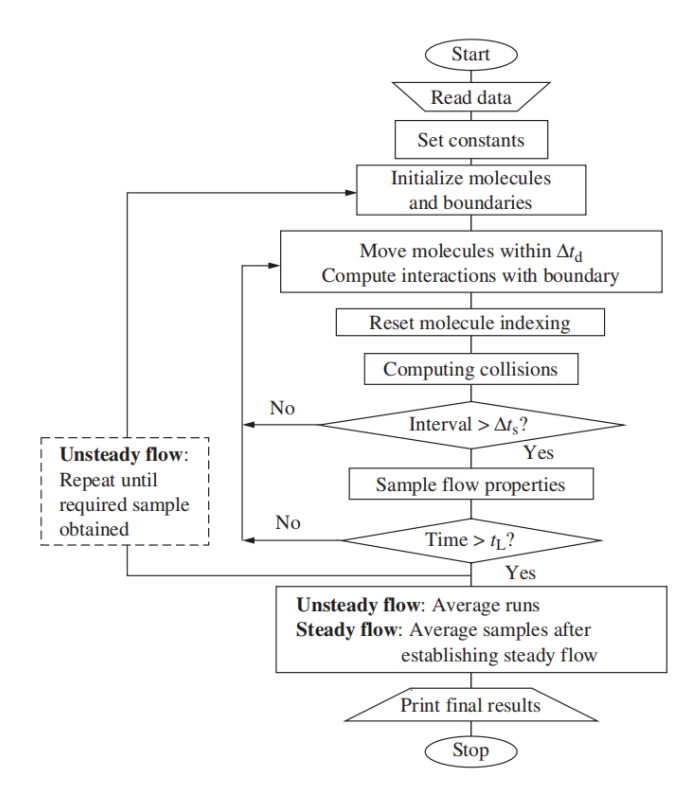


Figure 4 – DSMC Flowchart. [11]

- 4. **Collision:** Once the particles have been properly indexed, intermolecular collisions are determined. This process is statistically modeled, and only molecules located in the same computational cell are considered candidates for collision. From all possible collision pairs, a representative set of collisions is randomly selected. To ensure effective separation between molecular movement and collisions, Δt_d must be smaller than the average time between collisions.
- 5. Sampling: After repeating the steps of movement, indexing, and collision over an extended time interval, macroscopic properties are calculated. Since these steps are independent of the calculation process, sampling can be performed every certain number of time intervals. DSMC generates transient results, so if a steady-state solution is required, it is carried out for a sufficiently long time (tL) and the desired result is obtained by averaging the results after reaching stability. For transient solutions, averages of multiple independent simulations can be used.

An important part of how the method is applied is the way collisions are modeled and the sampling method used. In this study, a VHS model for collisions and the NTC technique for sampling are used, which are presented below.

3. Validation of dsmcFoam+ code

For the validation process, DSMC computations of the Apollo capsule were performed, and the obtained results were compared with those available by Moss [9]. In the present investigation, simulations of the Appolo capsule were conducted for 100, 150, and 200 km of altitude. The capsule geometry and the reference system is presented in the Figure 5a and Figure 8a.

The flow properties for the three altitudes under study are described in Table 1. In this table, can be observed the number density n_{∞} , the mass density ρ_{∞} , the temperature of the free flow T_{∞} , and the molecular mass. Additionally, the temperature of the capsule surface used in the simulations, denoted as T_W [K], is presented.

For all the simulations, the flow velocity was set to 9600[m/s] at an angle of attack of -25° . It was considered a non-reacting flow with three species (presented in Table 2) with constant surface temperature. The freestream properties used in each simulation is presented in Table 1.

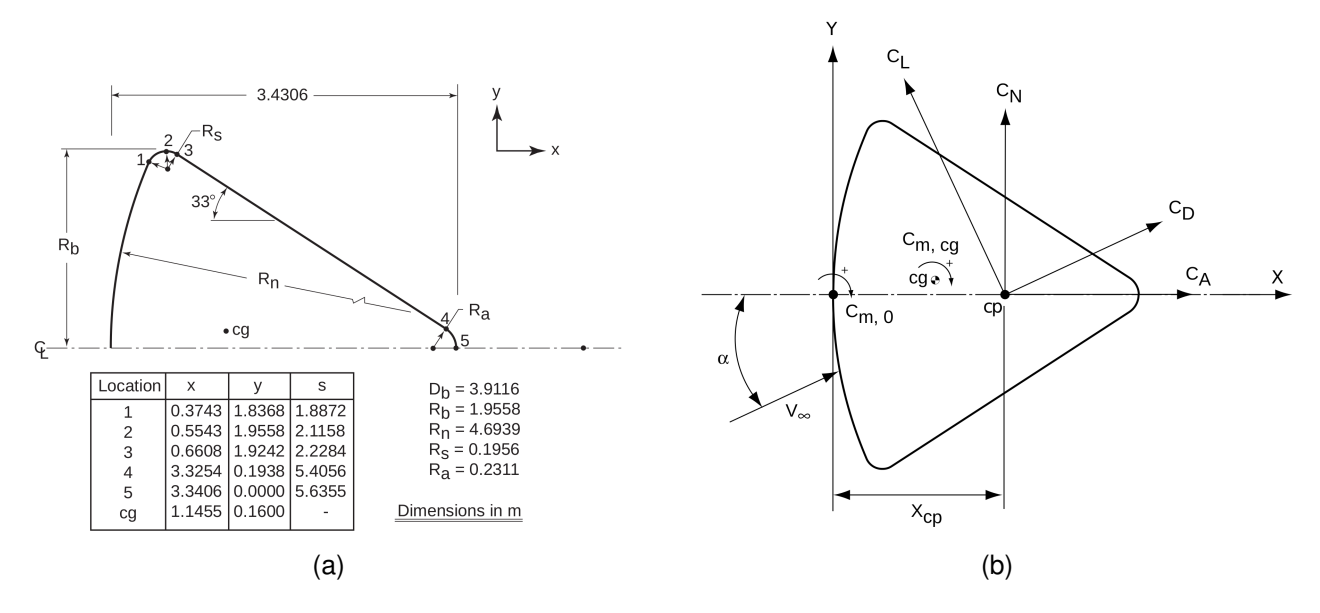


Figure 5 – Apollo capsule geometry (a) and reference system (b) [9].

Moreover, the Knudsen number for each simulation $(Kn_{\infty,D,HS})$ is presented in Table 2, this based on the mean free path λ_{∞} and the maximum diameter of the capsule D_b (shown in Figure 5a. Here, considering the Knudsen numbers and according to Figure 3, can be seen that the simulations are under slip flow, transition and free-molecular regimes for 100, 150, and 200[km], respectively. Furthermore, in the three conditions the flow can be considered hypersonic, due the mach numbers being above Mach 11, reaching even Mach 33 for 100 [km] altitude, all values above 5, the common value to define this kind of regime [12].

Altitude [km]	$n_{\infty} [m^{-3}]$	$\rho_{\infty} [kg/m^3]$	T_{∞} [K]	Molecular mass	$T_W[K]$
100	1.1898×10^{19}	5.5824×10^{-7}	194	28.258	1146
150	5.3055×10^{16}	2.1383×10^{-9}	733	24.273	373
200	8.9996×10^{15}	3.2829×10^{-10}	1026	21.970	234

Table 1 – Free-stream properties at 100, 150 and 200 [km] [9]).

Altitud [km]	X_{O2}	X_{N2}	X_O	$Kn_{\infty,D,HS}$
100	0.17683	0.78440	0.03877	0.0338
150	0.05461	0.61557	0.32982	7.59
200	0.03146	0.45476	0.51378	44.74

Table 2 – Atmospheric composition at 100, 150 and 200 [km] [9].

The computational domain is large enough to ensure it does not influence the flowfield structure close to the geometry. A vacuum boundary is applied at the outlet, positioned sufficiently far from the stagnation point. Additionally, due to the capsule axisymmetry, just half of the geometry is considered during the simulations.

Figure Figure 6a the boundary conditions used during the simulations: (I) represents the inlet where molecules enter and leave the computational domain; (II) represents a symmetry plane, where specular reflection is applied, and (III) diffuse wall with complete thermal accommodation.

The computational domain's cell size was chosen to be less than $0.5\lambda_{\infty}$ to follow good DSMC practice. A reference mesh is presented in Figure 6b. A refinement zone is observed near the capsule's geometry to improve surface mesh quality. These considerations result in computational meshes with different cell dimensions, domain volume and quantity of cells, these are listed in Table 3. Furthermore, the equivalent number of particles is calculated such that, on average, each cell contains 9 particles. The time step used in the simulations is calculated as a fraction of the mean collision time.

Table 3 the computational parameters used in each simulation.

Altitude [km]	Average cell length [m]	Volume [m ³]	No of cells	Time step [s]	Simulated time [s]
100	0.06	311.579	1438216	1.3 <i>e</i> – 6	0.13
150	0.19	9441.58	1287389	3.7e - 6	0.74
200	0.37	64791.6	1229056	2.6e - 6	2.561

Table 3 – Simulation parameters.

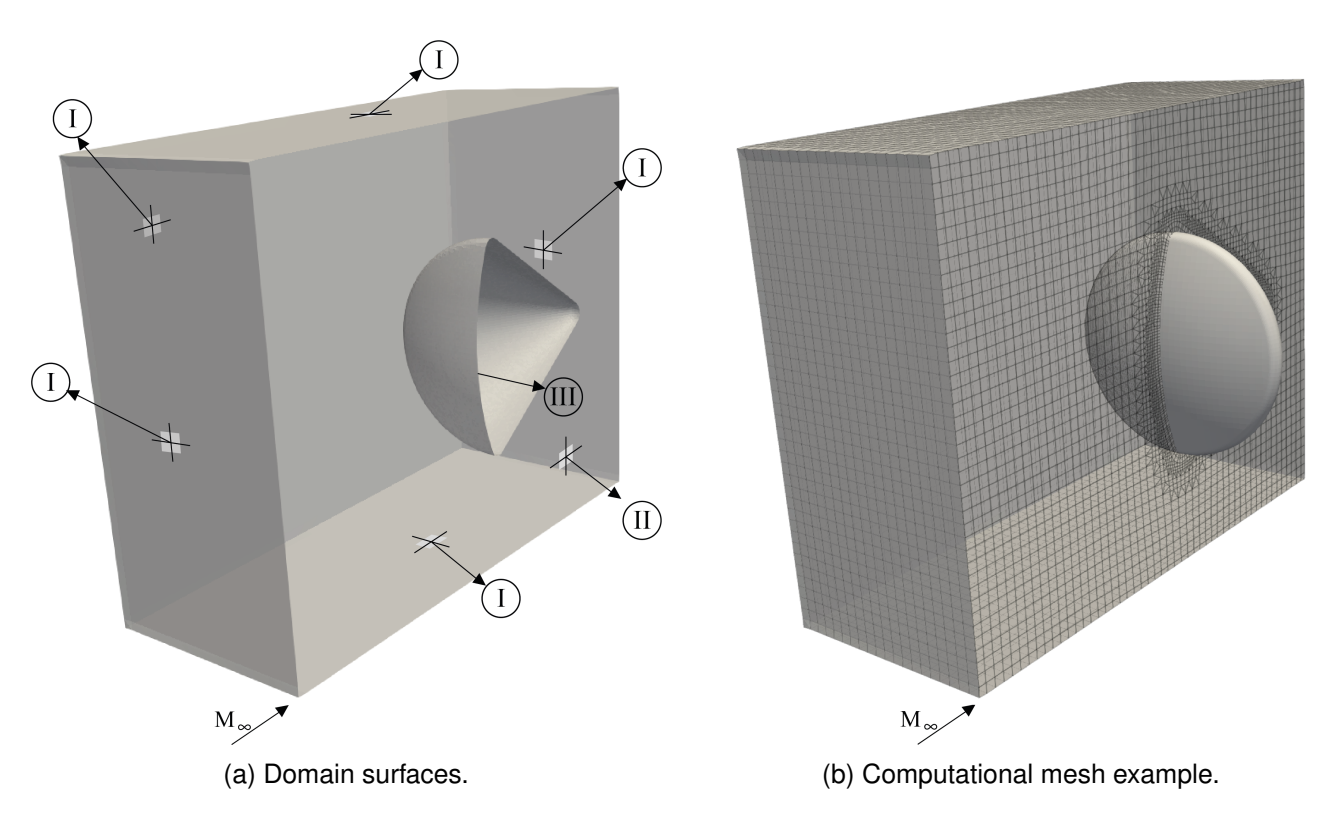


Figure 6 – Apollo capsule domain example.

Table 4 shows C_A , C_N , and $C_{m,0}$ obtained by the dsmcFoam+ calculations and those computed by DAC code. A good agreement between the results computed by both DSMC codes is observed.

Altitud		100 [km]		150 [km]) [km]			200 [km]	
Coef	Moss	dsmcFoam+	error	Moss	dsmcFoam+	error	Moss	dsmcFoam+	error	
C_A	1,448	1,405	2,97 %	1.723	1,685	2,21 %	1.731	1,718	0,75 %	
C_N	-0,279	-0,275	1,43 %	-0.757	-0,713	5,81 %	-0.777	-0,762	1,93 %	
$C_{m,0}$	0,109	0,108	0,92 %	0.113	0,111	1,77 %	0.113	0,112	0,88 %	

Table 4 – Aerodynamic coefficients Apollo.

4. Geometry definition and computational parameters

The DHS geometry used in the present investigation is shown in Figure 7. It consists of a 16U CubeSat with a mechanically deployable heat shield with 8 movable flaps to control the satellite during reentry through the atmosphere. Once deployed, this system has a diameter of 1.5 meters with an approximate mass of 40 kg.

The present work investigates the influence of altitude on the flowfield structure around the DHS. The altitudes considered in this work ranges from 200 to 200 km altitude. The freestream properties used in each simulation are presented in Table 5. The flow reentry velocity is set to $7800 \, [\text{m/s}]$ at an angle of attack of 0° for all simulations. In addition, it is considered a non-reactive hypersonic flow

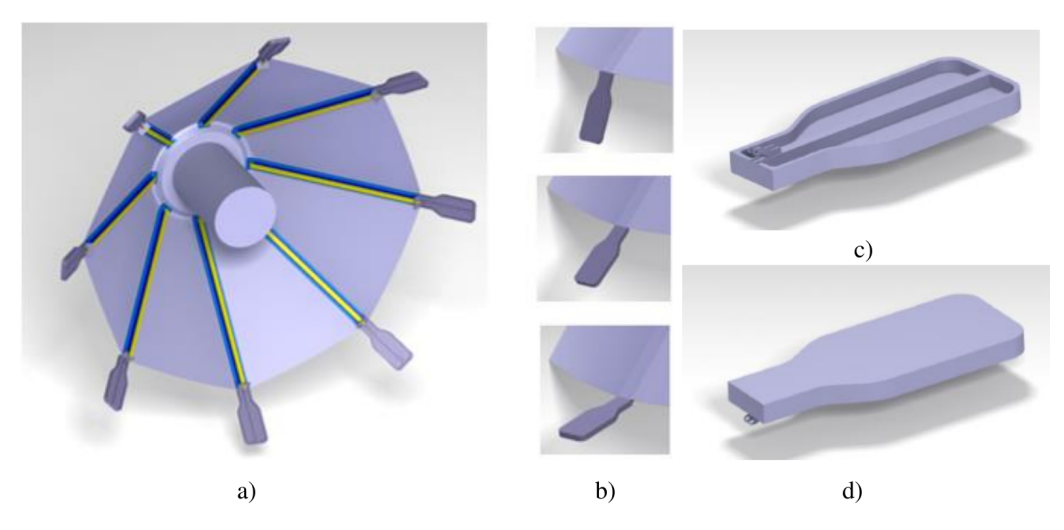


Figure 7 – DHSs with flaps geometry. [8]

composed of three species with different compositions, as shown in Table 6). The geometry surface temperature was assumed to be constant and equal to 1000~[K] for the three altitudes. Considering the DHS maximum diameter, the Knudsen numbers are 0.095, 22, and 160~for 100, 150, and 200~[km] altitude, respectively. In doing so, the DSMC computations are performed under slip-flow, transition, and free-molecular regimes.

Altitude [km]	$n_{\infty} [m^{-3}]$	$\rho_{\infty} [kg/m^3]$	T_{∞} [K]	$\lambda_{\infty}[m]$	M [kg/kmol]
100	1.189×10^{19}	5.604×10^{-7}	195.08	1.42×10^{-1}	28.40
150	5.186×10^{16}	2.076×10^{-9}	634.39	3.3×10^{1}	24.10
200	7.182×10^{15}	2.541×10^{-10}	854.56	2.4×10^{2}	21.30

Table 5 – Free-stream properties at 100, 150 and 200 [km] [13]).

Altitude [km]	n_{N2}	n_{O2}	n_O
100	9.210×10^{18}	2.151×10^{18}	4.298×10^{17}
150	3.124×10^{16}	2.750×10^{15}	1.780×10^{16}
200	2.925×10^{15}	1.918×10^{14}	4.050×10^{15}

Table 6 – Atmospheric composition at 100, 150, and 200 km altitude [13].

In order to decrease the computational time, a quarter of the geometry is considered in all simulations. Figure 8 a) shows the boundaries employed during the computations: (I) inlet boundary condition; (II) a vacuum boundary; (III) symmetry plane; and (IV) diffuse reflection with complete thermal accommodation is used.

Figure 8b shows the mesh used for the DSMC computation at 100 km altitude. This figure shows that mesh refinement is applied near the DHS surface to improve the capture of the physical phenomena near the body. The mesh is designed to balance precision and computational time well, accomplishing the method requirement. The cell size is chosen to be less than $0.5\lambda_{\infty}$ and contains, in average, 9 DSMC particles per cell. The time step is calculated as a fraction of residence time. To accommodate the shock wave inside the computational domain, different meshes were used for each altitude considered in this investigation, as shown in Table 7.

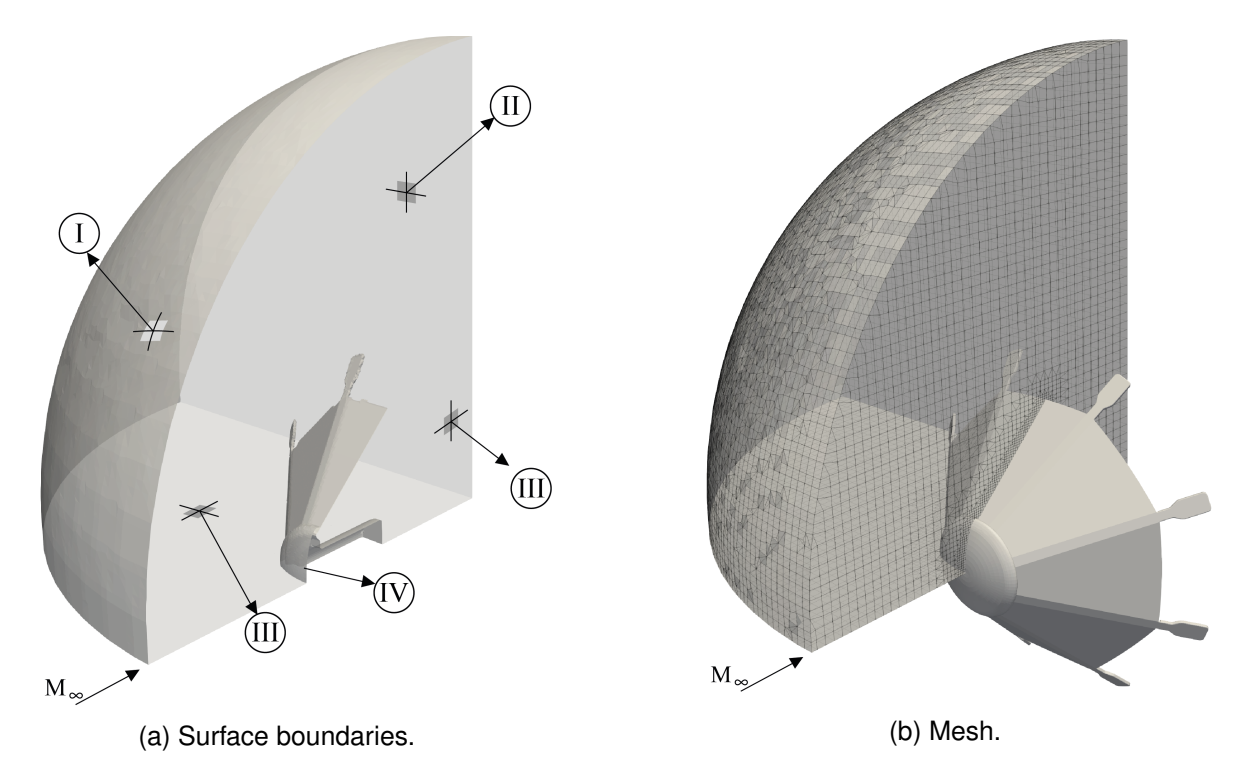


Figure 8 – Reference DHS mesh and surfaces.

Altitude [km]	Average cell length [m]	Volume [m ³]	No. of cells	Time step [s]	Simulated time [s]
100	0.015	7.12	1945801	6.8e - 7	0.0884
150	0.048	220	2020758	1.13e - 6	0.32205
200	0.049	263	2274707	1.25e - 6	0.45

Table 7 – DHS simulation parameters.

5. Computational results and discussion

In this section, the influence of altitude during the reentry of a satellite coupled with DHS is discussed in detail. The macroscopic properties considered in this investigation are velocity, temperature, mass density, and pressure. The contour plots and macroscopic distribution along the stagnation streamline are presented for 200, 150, and 100 km altitude.

5.1 Velocity flowfield

Figure 9, 12, and 14 shows the velocity contours with streamlines. In addition, Figure 11 and 13 depicts the velocity contours close to the DHS surface. According to this figure, the flow enters the domain at 7800 m/s and decelerates as the flow moves toward de DHS. The velocity flow decrease exhibits different structures and magnitudes depending on the altitude and rarefaction level. The velocity decrease towards the DHS is attributed to the high collision rate near the surface.

At 100 [km] altitude, a rapid deceleration of the flow can be noticed. Considering the stagnation line, the flow is decelerated to 0 m/s in less than 1 m, with a significant gradient near the surface. A thin low-velocity zone surrounding all the capsule surfaces, from the nose to the back.

A different flow structure is observed for the altitudes of 150 and 200 km. Since the shock wave is more diffuse for these altitudes, it takes approximately 9 and 11 m to completely decelerate the flow, with a gradual deceleration and a small velocity gradient compared to the 100 km case. In addition, the low-velocity zone upstream for both cases is bigger than the 100 [km] case; however, this zone is not continuous from the nose to the back of the capsule. At the shoulder, there is a region of the high-velocity gradient after the floe separation, and a low-velocity region is formed at the wake.

The velocity for the three cases along the stagnation line is shown in Figure 10. It is noticed a significant difference between flow distribution along the stagnation streamline for 100, 150, and

200 km cases. The presence of the capsule affects further upstream flow due to increased flow rarefaction.

The flow around the DHS shoulder also depends on the rarefaction level. For cases at 150 and 200 km, it is a critical region where the flow abruptly expands into the wake. A low-velocity wake is formed behind the DHD, and no recirculation zone is observed for the altitudes considered in this investigation.

On the other hand, for the case of 100 [km], small gradients with smooth flow variations are observed. Although there is a flow expansion after the shoulder, it is not abrupt. Additionally, there is a transition zone between the low-velocity wake and the high-velocity zone, but it is wider and more diffuse than that for 150 and 200 [km].

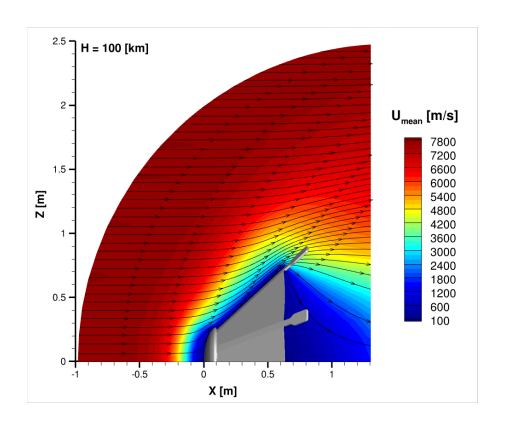


Figure 9 – Velocity contour for 100[km]

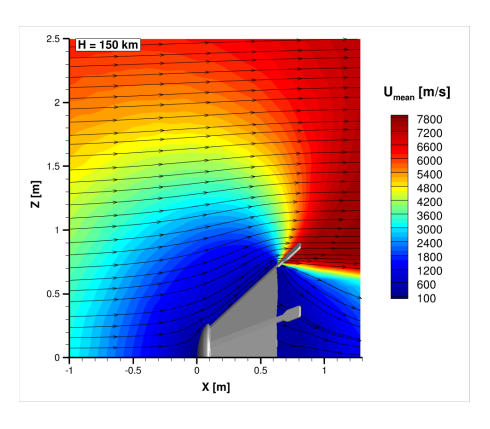


Figure 11 – Velocity contour for 150[km] (zoom)

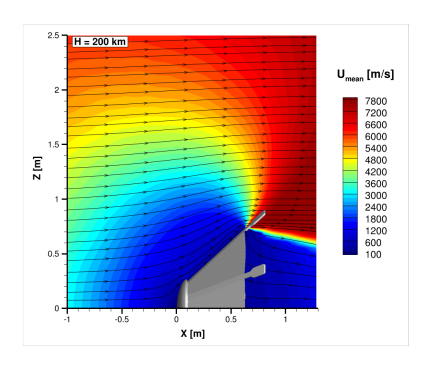


Figure 13 – Velocity contour for 200[km] (zoom)

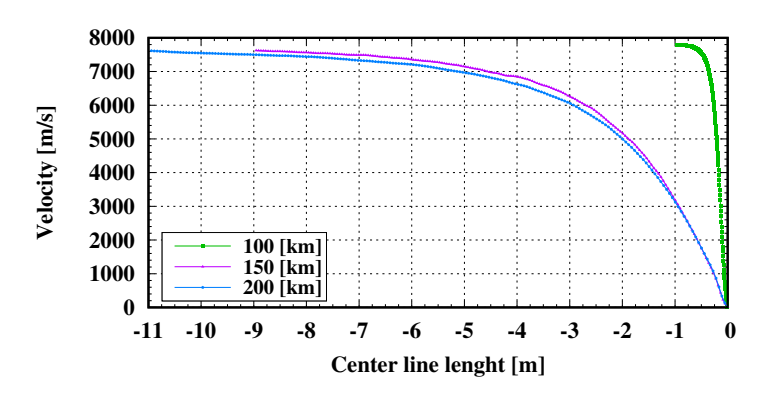


Figure 10 – Velocity along stagnation streamline

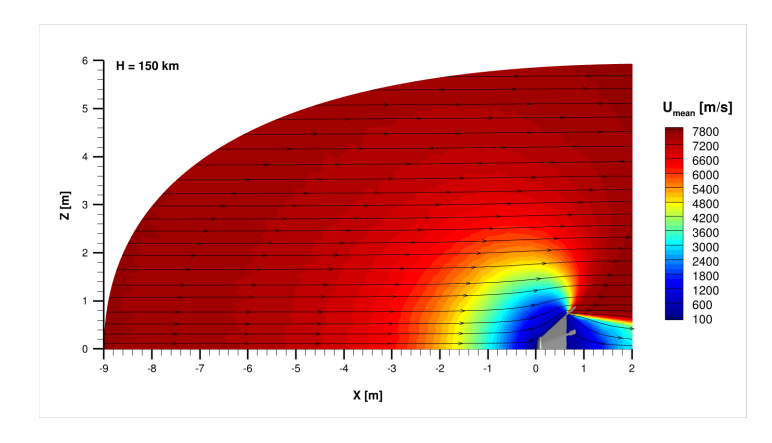


Figure 12 – Velocity contour for 150[km].

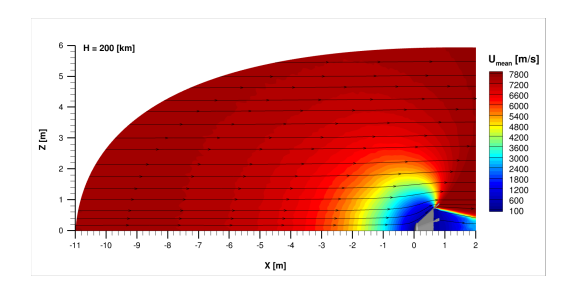


Figure 14 – Velocity contour for 200[km].

5.1.1 Temperature flowfield

Figure 15, 18 and 20 show the temperature contours during the reentry from 200 to 100 km. Similar to velocity countors, Figure 17 and Figure 19 show the temperature contours near the body.

According to the plots, a high-temperature shock wave is formed upstream of the DHS. At 200 km altitude, a very diffuse shock wave is observed, in which the high-temperature regions expand up to -5.0 m upstream of the stagnation point. As the satellite, coupled with the DHS, moves towards a thincking atmosphere, the shock wave gets close to the DHS surface. At 150 and 100 km altitude, the high-temperature shock wave expands to -4.0 and 0.4 m upstream at the DHS stagnation point. In addition, as the flow expands into the wake, a low-temperature region is observed beside the DHS, from 0.8 to 1.5 m, and a significant increase after 1.5 m due to the flow compression.

Figure 16, shows the translational temperature distribution along the stagnation streamline. In this plot is clear the influence of the altitude on the temperature field. from 200 to 150 km altitude. At 100 km, the shock wave peak temperature occurs near the DHS surface, where the higher temperature zone has a thickness of 0.2 m and a peak temperature of 26000 K at 0.15 m from the stagnation point. The peak temperature is 133 times the freestream temperature for that altitude.

Still referring to Figure 16, the shock wave is much more diffuse at 150 and 200 km altitude. The high-temperature zones have thicknesses of 1.9 [m] and 2.1 m, with maximum temperature values surrounding the 18500 [K] and 17000 [K] at 1.1 [m] and 1.15 [m] for 150 and 200 km, respectively. The peak temperature was 29 and 19 times the T_{∞} for 150 and 200 km, respectively.

The difference in temperatures reached at different altitudes, as well as the size of the high-temperature zones, are directly related to the rarefaction of the flow. For 100 km, where the mean free path is short, and the collision rate is high, particles travel a small distance before colliding with each other after being reflected by the capsule. Additionally, the number of collisions is higher, reducing the distance from the point of maximum temperature but increasing its magnitude. On the other hand, for the cases of 150 and 200 km, with low collision rates and increased mean free path, particles travel a longer distance to produce a collision at lower collision rate. This results in a more diffuse heating with lower maximum temperatures.

The shock wave structure at 100 [km] surrounds the nose and the heat shield, extending parallel to it beyond the body of the capsule. In addition, there exists a cold zone near the surface of the DHS, such that the heat generated at the hottest point is not directly transferred to the body. Instead, due to the flow stagnation near the wall, a thermal barrier is formed around the capsule (this will be more evident when analyzing pressure contours). It is also important to note that it rapidly cools once the flow moves away from the capsule downstream.

For higher altitudes, the shockwave structure also surrounds the nose and DHS surface. However, similar to the velocity plots, the shoulder is a critical point where the shockwave converges. This results in very high temperatures near the surface and a high gradient, such that downstream from the shoulder, there is a sudden cooling of the flow. Also, low temperatures are observed behind the capsule in the stagnation zone. However, shortly after, the formation of a medium-temperature wake generated at the shoulder can be observed (this is more noticeable for 150 km). Similarly to the case of 100 km, a low-temperature zone near the surfaces of the DHS is observed, but it is much more diffuse.

For the higher altitude cases, the abrupt temperature decrease after the shoulder is due to the rapid expansion in the flow (seen in velocity contours) and, consequently, the lack of particle collisions due to the high mean free path. On the other hand, the thermal wake produced also correlates with velocity, where a thermal transition zone is produced because the expansion is slower (transition zone between high and low velocity). Here, the flow energy not converted into velocity transforms into heat.

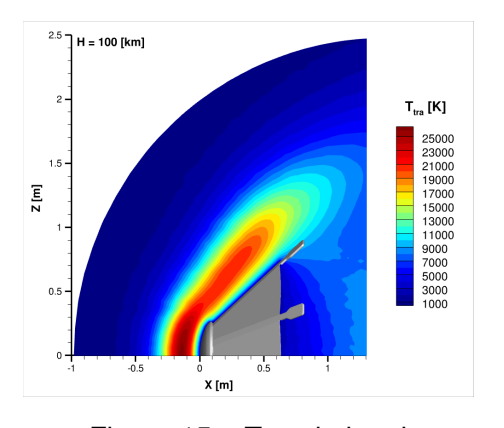


Figure 15 - Translational

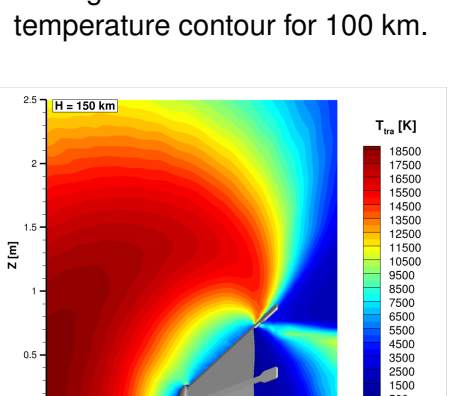


Figure 17 - Translational temperature contour for 150 km.

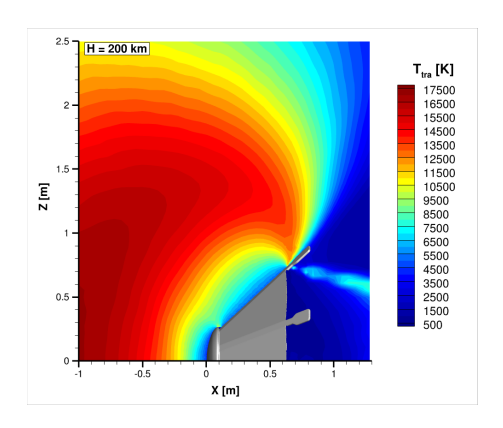


Figure 19 - Translational temperature contour for 200km

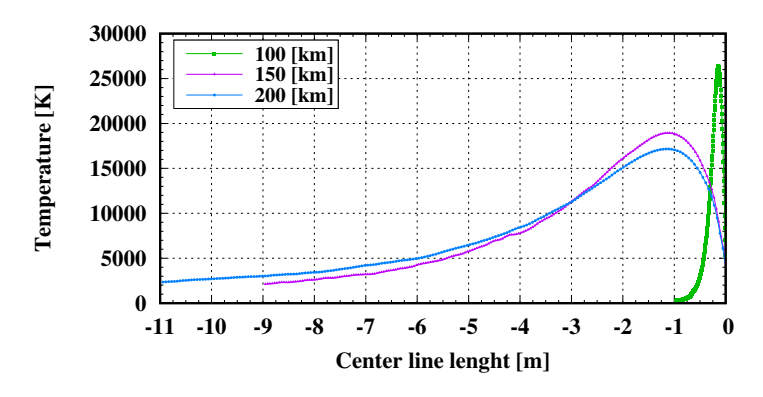


Figure 16 – Translational temperature distribution along stagnation line.

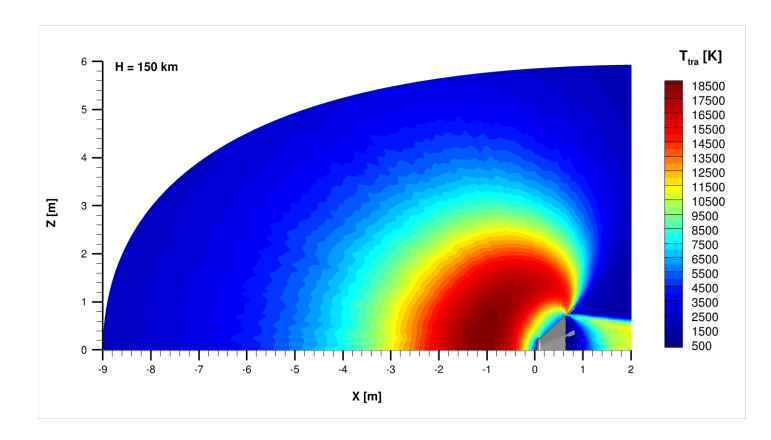


Figure 18 – Translational temperature contour for 150 km.

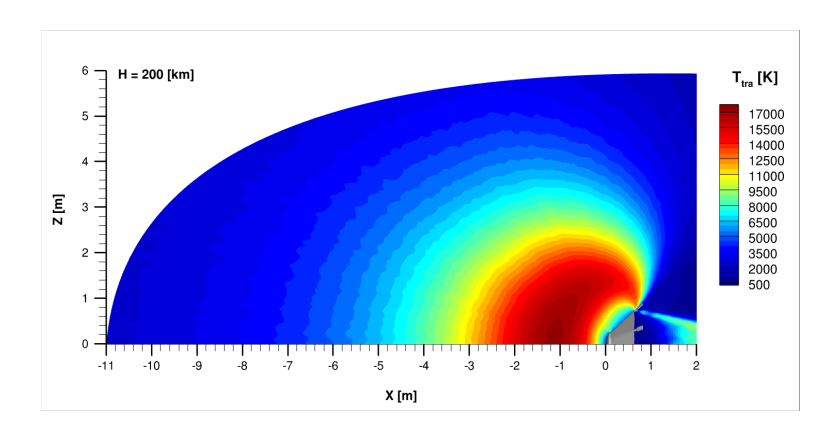


Figure 20 – Translational temperature contour for 200 km

5.1.2 Mass density flowfield

Mass density contours are presented in Figure 21, 24, and 26. In addition, a closer view is presented for higher altitudes at Figure 23 and 25. It is important to note that all contours are presented on a logarithmic scale.

It can be observed that the mass density of the free flow varies by several orders of magnitude between the different altitudes studied due to flow rarefaction. This can also be seen in Figure 22, where the exponential growth of mass density near the stagnation point can be noted for the three altitudes. Here, a slow increase in density away from the body can also be observed, where it remains almost constant until it is nearly in contact with the DHS.

For 100 m, it can be seen that a high-density region is formed close to the surface, ranging from 0

to 0.25 m upstream from the stagnation point and surrounding the entire surface of the DHS up to the shoulder. The highest density values are found over the surface of both the nose and the DHS surface, reaching values of 4×10^{-5} [kg/m^3], 71 times the value for the free flow.

Similar to the other macroscopic properties analyzed, it is noticed at 150 and 200 km that an increase in density becomes considerable from 2 to 3 m upstream from the stagnation point, respectively. The shock wave is more diffuse for these altitudes; however, the high-density region occurs over the DHS surface for all the altitudes considered in this work. For 150 and 200 km altitude, the peak value of mass density is 5×10^{-8} and 5×10^{-9} [kg/m^3], which corresponds to 24 and 19 times the ρ_{∞} , respectively.

Once again, the difference in structures for the different altitudes is explained by the varying degrees of flow rarefaction. A greater mean free path leads to a lower collision rate, so reflected particles travel further before colliding with one another, explaining the diffuse effect of 150 and 200 km. On the other hand, the opposite occurs for 100 [km], where the lower degree of rarefaction results in a shorter mean free path, leading to many collisions closer to the surface.

Furthermore, it should be noted that the high density produced near the surface is due to the flow being at a lower velocity and with a higher collision rate, thereby retaining a greater number of particles. Finally, a low density can be observed in the small space between the nose and the DHS surface at three altitudes considered in the present investigation. This is caused by the flow direction, which at that point is parallel to the end of the nose curve. Due to the high density at the nose and the higher collision rate, the flow tends to maintain its direction. As a result, a pressure difference occurs, pushing particles away from this space and preventing them from entering this small volume.

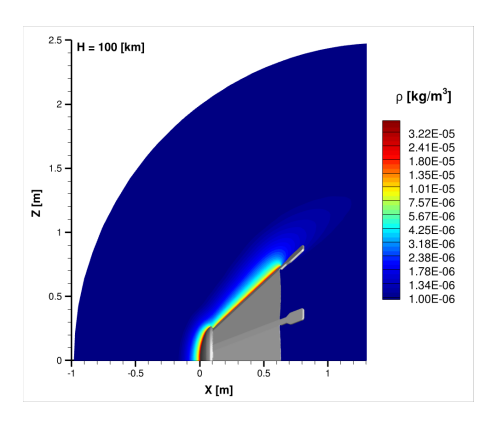


Figure 21 – Mass density contour for 100 km.

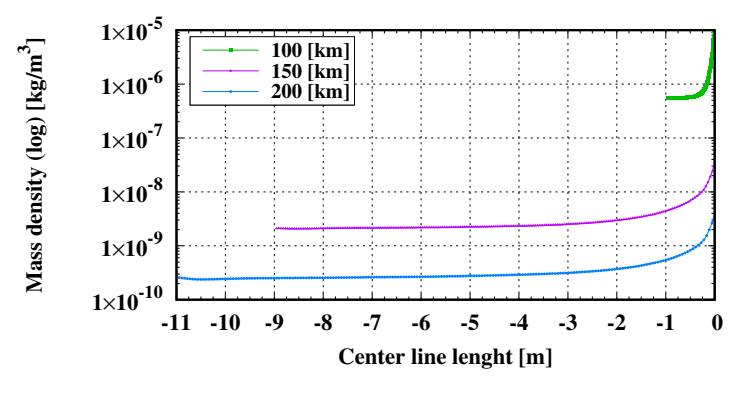


Figure 22 – Mass density distribution along stagnation line.

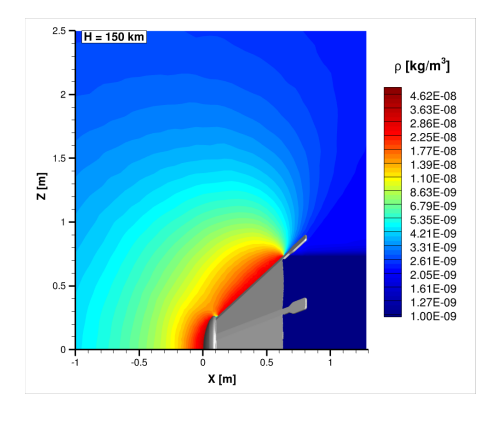


Figure 23 – Mass density contour for 150 km.

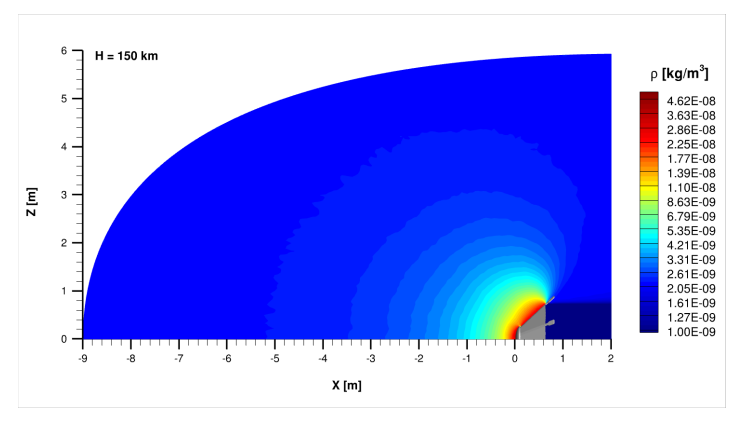


Figure 24 – Mass density contour for 150 km.

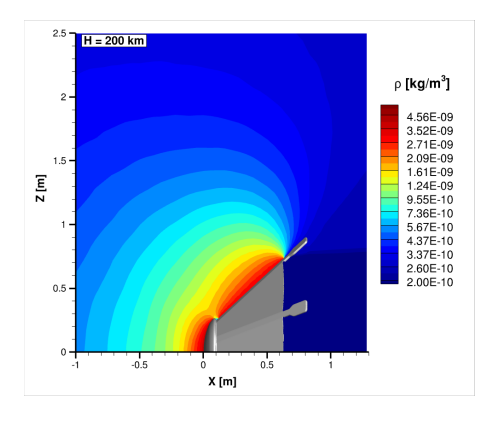


Figure 25 – Mass density contour for 200 km.

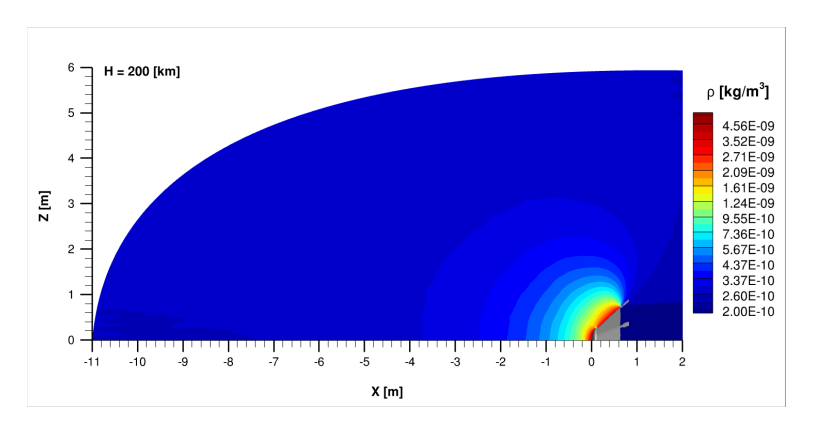


Figure 26 – Mass density contour for 200 km.

5.1.3 Pressure flowfield

Figure 27, 30 and 32 can be seen the contours of pressure for the three altitudes. Additionally, the closer views are presented in Figure 29 and 31. As occurred with density, due to the rapid growth of pressure near the surface and the difference in magnitudes for the different cases, the results are presented on a logarithmic scale.

For 100 km, a similar structure to that present at the same altitude can be observed in the density contour but more diffuse. It also reaches its maximum on the walls bordering the mantle and nose of the body. On the other hand, compared to density, pressure exhibits exponential growth throughout the domain, not just in the closest sector of the DHS; however, this growth is less perceptible away from the walls due to its magnitude and the high values found on the surface itself.

For 150 and 200 km, we also find similar shapes to the density contours but more diffuse. However, like at 100 km, there is growth throughout the domain but with a lower gradient. Again, the maximum values are found on the surface, with an exponential gradient.

It is worth noting that the maximum pressure values for all three cases are present at the stagnation point, reaching values greater than 38.98, 0.1468, and 0.017832 [Pa], corresponding to 1217, 323, and 210 times P_{∞} for 100, 150, and 200 [km], respectively.

The pressure values along the stagnation line for the three cases can be directly compared in Figure 28. Here, the exponential growth of pressure throughout the domain can be appreciated, as well as the difference in magnitude of pressure for the studied altitudes.

The increase in pressure near the surface is caused by several factors. Near the wall, there is the stagnation zone, where higher density and lower flow velocity result in an increased collision rate, leading to more particles colliding with the surface and thus increasing pressure. Additionally, considering the macroscopic properties near the surface, there is little kinetic energy due to stagnation, and, as previously seen, the temperature is relatively low. Therefore, the thermal energy of the flow at that point is also low, with a significant portion of the flow energy being in the form of pressure.

The difference between the maximum pressures at different altitudes can also be explained by considering the collision ratio for each case. With lower rarefaction, the collision ratio is higher, increasing the number of particles colliding with the wall considerably, thus increasing the pressure on the surface.

Finally, as mentioned in the previous section, there is a small gap between the mantle and the nose where there is low density and pressure. This is due to the low concentration of particles entering this cavity due to the flow direction, causing a low collision rate and, therefore, lower pressure.

6. Conclusions

In this research, the Direct Simulation Monte Carlo (DSMC) method was employed using dsmcFoam+ to evaluate the effect of altitude on the rarefied flow structure around a Deployable Heat Shield (DHS) with an aerodynamic control system based on 8 flaps specifically designed for the reentry and recovery of a 16U CubeSat. This approach was selected due to computational fluid dynamics (CFD) limitations for rarefied flows, necessitating a molecular approach based on the Boltzmann equation.

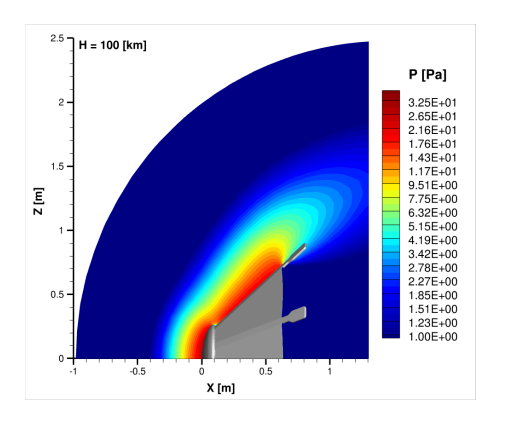


Figure 27 – Pressure contour for 100 km.

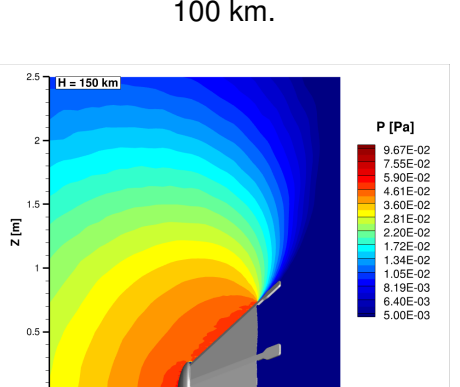


Figure 29 – Pressure contour for 150 km.

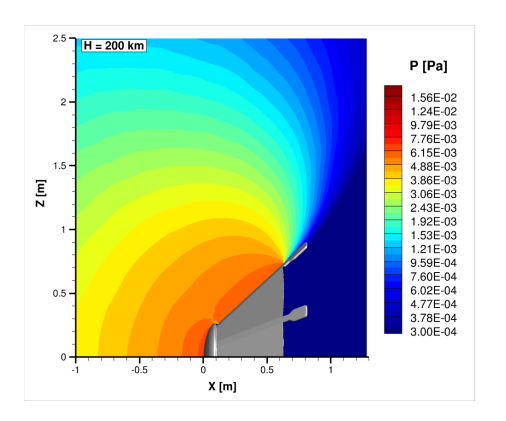


Figure 31 – Pressure contour for 200 km.

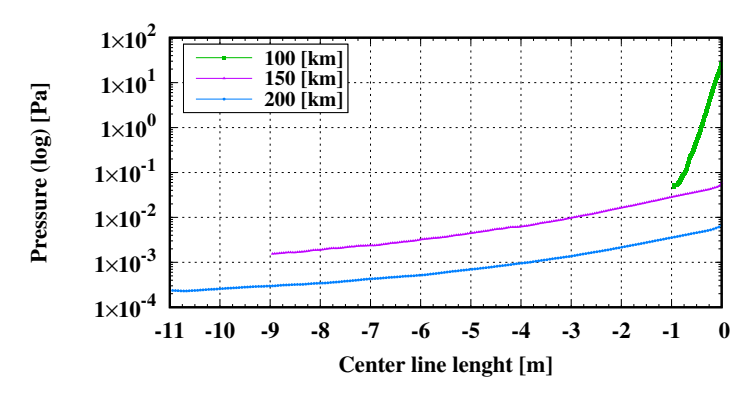


Figure 28 – Pressure distribution along stagnation line.

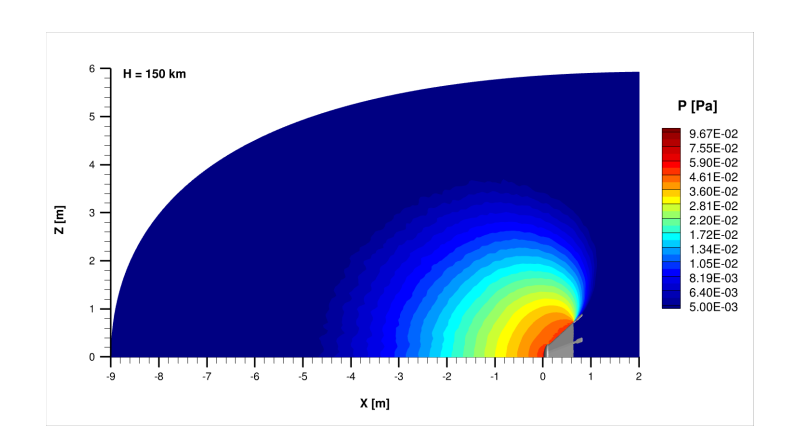


Figure 30 – Pressure contour for 150 km.

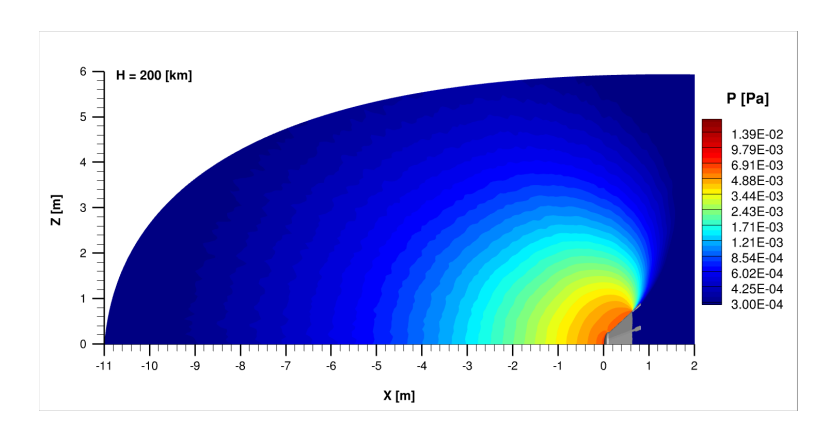


Figure 32 – Pressure contour for 200 km.

A validation process was carried out to ensure the capability of the dsmcFoam+ code to resolve hypersonic rarefied flows without considering chemical reactions. The results obtained with the dsmcFoam+ code for the flow around the Apollo capsule at different altitudes were compared with those obtained by Moss in 2006 [9], revealing good agreement between both data sets.

Once validated, the code was used to understand the flow structure around the DHS during atmospheric reentry at three altitudes of interest: 100, 150, and 200 km. The formation of a diffuse shock wave upstream of the DHS was observed, along with significant changes in temperature, pressure, and density over the studied system, where the shock wave became less diffuse as the vehicle penetrated the atmosphere.

While the similarity in flow structures for 150 and 200 km can be seen, there is a significant difference between these results and those obtained for 100 km. Much more diffusivity is observed at higher

altitudes, and different flow structures are present. The gap behind the nose and the shoulder are points of interest due to the flow division and the high gradients near these areas.

For all altitudes, a stagnation point can be seen at the center of the nose, where low temperatures and velocities but high pressures and densities are recorded. The effect of flow rarefaction shows that at lower altitudes, the impacts on the reentry system, such as maximum temperature, pressures, and flow deceleration, are greater.

This research significantly contributes to understanding the aerodynamics of DHSs for protecting and recovering CubeSats during atmospheric reentry. The results obtained are valuable for designing and developing thermal protection systems for future space missions.

7. Contact Author Email Address

rodrigo.cassineli@usm.cl

8. Copyright Statement

The authors confirm that they, and/or their company or organization, hold copyright on all of the original material included in this paper. The authors also confirm that they have obtained permission, from the copyright holder of any third party material included in this paper, to publish it as part of their paper. The authors confirm that they give permission, or have obtained permission from the copyright holder of this paper, for the publication and distribution of this paper as part of the ICAS proceedings or as individual off-prints from the proceedings.

References

- [1] Jones H. The recent large reduction in space launch cost. 48th International Conference on Environmental Systems, 2018.
- [2] Bomani B. M. Cubesat technology past and present: Current state-of-the-art survey. Technical report, 2021.
- [3] Carná S. R and Bevilacqua R. High fidelity model for the atmospheric re-entry of cubesats equipped with the drag de-orbit device. *Acta Astronautica*, 156:134–156, 2019.
- [4] Hughes S, Cheatwood F, Dillman R, Calomino A, Wright H, DelCorso J, and Calomino A. Hypersonic inflatable aerodynamic decelerator (hiad) technology development overview. In *21st AIAA Aerodynamic Decelerator Systems Technology Conference and Seminar*, page 2524, 2011.
- [5] Longo J and Radespiel R. Flap efficiency and heating of a winged re-entry vehicle. *Journal of spacecraft and rockets*, 33(2):178–184, 1996.
- [6] Bird G. Molecular gas dynamics and the direct simulation of gas flows. Clarendon Press, 1994.
- [7] White C, Borg M. K, Scanlon T. J, Longshaw S. M, John B, Emerson D. R, and Reese J. M. dsmcfoam+: An openfoam based direct simulation monte carlo solver. *Computer Physics Communications*, 224:22–43, 2018.
- [8] Gaglio E, Cecere A, Guida R, Mungiguerra S, Savino R, Caqueo Jara N, and Cassineli Palharini R. Aerodynamic analysis of a flap-based deployable re-entry system in different flight conditions. In *25th AIAA International Space Planes and Hypersonic Systems and Technologies Conference*, page 16, 2023.
- [9] Moss J, Glass C, and Greene F. Dsmc simulations of apollo capsule aerodynamics for hypersonic rarefied conditions. *Collection of Technical Papers 9th AIAA/ASME Joint Thermophysics and Heat Transfer Conference Proceedings*, 3, 06 2006.
- [10] Hak M. Mems: introduction and fundamentals. CRC press, 2005.
- [11] Fang Y. *Microfluid mechanics: Principles and modeling. nanoscience and technology series.* McGraw-Hill Pub., 2006.
- [12] Bertin J. J. Hypersonic aerothermodynamics. AIAA, 1994.
- [13] Administration A and Standard Atmosphere U. S. C. *Us standard atmosphere, 1976.* National Oceanic and Amospheric [sic] Administration, 1976.